

# Generalized Parton Distributions from Deep Virtual Compton Scattering at CLAS.

M. Guidal

*Institut de Physique Nucléaire d'Orsay, 91405 Orsay, France*

(Dated: August 27, 2018)

We have analyzed the beam spin asymmetry and the longitudinally polarized target spin asymmetry of the Deep Virtual Compton Scattering process, recently measured by the Jefferson Lab CLAS collaboration. Our aim is to extract information about the Generalized Parton Distributions of the proton. By fitting these data, in a largely model-independent procedure, we are able to extract numerical values for the two Compton Form Factors  $H_{Im}$  and  $\bar{H}_{Im}$  with uncertainties, in average, of the order of 30%.

PACS : 13.60.Le, 13.60.Fz, 13.60.Hb

arXiv:1003.0307v1 [hep-ph] 1 Mar 2010

The study of Generalized Parton Distributions (GPDs) is currently one of the most intense fields of research in hadronic physics, theory-wise as well as experiment-wise. GPDs give access in an unprecedented way to part of the complex composite structure of the nucleon (or more generally of hadrons), which, until now, is not fully calculable from first principles of Quantum Chromo-Dynamics (QCD). For instance, nucleon GPDs encode, in a frame where the nucleon has a quasi-infinite momentum in a certain direction (the so-called “infinite momentum frame”), the longitudinal momentum distributions of the quarks and gluons in the nucleon, their transverse spatial distribution and, overall, the correlation between these two latter distributions, which is brand new information. As a consequence of this longitudinal momentum-transverse space correlations, there is the possibility to access the contribution of quarks to the orbital momentum of the nucleon. This is of great interest for the notorious “spin puzzle” of the nucleon, a long-standing issue in nucleon structure studies. We refer the reader to Refs. [1–8] for the original theoretical articles and recent comprehensive reviews on GPDs and for details on the theoretical formalism.

Nucleon GPDs are the structure functions which are accessed, through the factorisation property of QCD, in the hard exclusive electroproduction of a meson or a photon off the nucleon. If we focus on quark GPDs, the golden channel to access them is the Deep Virtual Compton Scattering (DVCS) process, due to the purely electromagnetic nature of the perturbative part of the “handbag” diagram. This latter diagram is schematized in Fig. 1. At large  $Q^2 = (e' - e)^2$  and small  $t = (p - p')^2$ , this process in which the same quark (or antiquark) absorbs the incoming virtual photon and radiates the final real photon, is predicted to be the dominant one. The quantities  $x + \xi$  and  $x - \xi$  are the longitudinal momentum fractions of the initial and final quark (or antiquark) respectively, where  $\xi = \frac{x_B}{2 - x_B}$  and  $x_B = \frac{Q^2}{2m\nu}$  (with  $\nu = E_{e'} - E_e$ ) is the standard Deep Inelastic Scattering (DIS) variable.

For DVCS on the proton, several experimental observables measured in different kinematical regimes have been published this past decade : cross sections (beam-polarized and unpolarized) from the JLab Hall A collaboration [9], beam spin asymmetries (BSA) [10, 11] and longitudinally

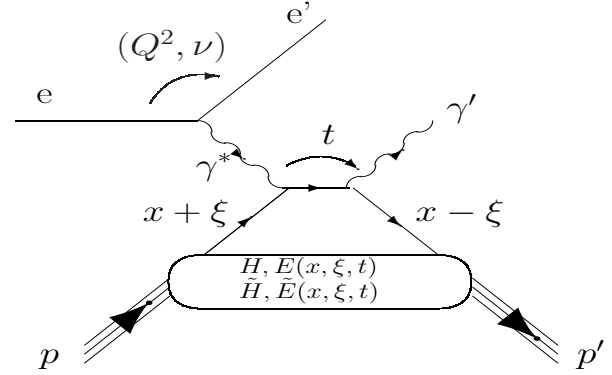


FIG. 1: The handbag diagram for the DVCS process on the proton  $ep \rightarrow e'p'\gamma'$ . There is also a crossed diagram which is not shown here.

inally polarized target asymmetries (ITSA) [12] from the CLAS collaboration and a series of correlated beam-charge, beam-spin and transversely polarized target spin asymmetries from the HERMES collaboration [13–15]. The question arises: from this large harvest of experimental observables, with still much more to come, how can the GPD information be extracted? The issue is not trivial as we recall that:

- the Bethe-Heitler (BH) process is another mechanism which leads to the same final state  $ep \rightarrow ep\gamma$  as DVCS. In the BH process, the final state photon is radiated by the incoming or scattered electron and not by the nucleon itself. Therefore, the BH process, which dominates the cross sections in some kinematic regions, carries no information about GPDs. However, it is relatively precisely calculable in Quantum Electro-Dynamics (QED) given the nucleon form factors, which are quite precisely known at the kinematics we are presently interested in, i.e. small  $t$ .
- in the QCD leading twist and leading order approximation, which is the frame of this study, there are,

for DVCS, four independent GPDs:  $H$ ,  $E$ ,  $\tilde{H}$  and  $\tilde{E}$  which correspond to the various spin and helicity orientations of the quark and nucleon in the handbag diagram. These four GPDs depend on three variables  $x$ ,  $\xi$  and  $t$ . Decomposing the DVCS amplitude into real and imaginary parts leads to eight GPD-related quantities. We will call them the Compton Form Factors (CFFs) and they are the quantities which can in principle be extracted from DVCS experiments. Following our conventions introduced in Refs. [16, 17], these eight CFFs are:

$$H_{Re} = P \int_0^1 dx [H(x, \xi, t) - H(-x, \xi, t)] C^+(x, \xi) \quad (1)$$

$$E_{Re} = P \int_0^1 dx [E(x, \xi, t) - E(-x, \xi, t)] C^+(x, \xi) \quad (2)$$

$$\tilde{H}_{Re} = P \int_0^1 dx [\tilde{H}(x, \xi, t) + \tilde{H}(-x, \xi, t)] C^-(x, \xi) \quad (3)$$

$$\tilde{E}_{Re} = P \int_0^1 dx [\tilde{E}(x, \xi, t) + \tilde{E}(-x, \xi, t)] C^-(x, \xi) \quad (4)$$

$$H_{Im} = H(\xi, \xi, t) - H(-\xi, \xi, t), \quad (5)$$

$$E_{Im} = E(\xi, \xi, t) - E(-\xi, \xi, t), \quad (6)$$

$$\tilde{H}_{Im} = \tilde{H}(\xi, \xi, t) + \tilde{H}(-\xi, \xi, t) \quad \text{and} \quad (7)$$

$$\tilde{E}_{Im} = \tilde{E}(\xi, \xi, t) + \tilde{E}(-\xi, \xi, t) \quad (8)$$

with

$$C^\pm(x, \xi) = \frac{1}{x - \xi} \pm \frac{1}{x + \xi}. \quad (9)$$

In the QCD leading twist and leading order approximation, these eight CFFs depend only on  $\xi$  (or equivalently  $x_B$ ) and  $t$ .

In Refs. [16, 17], we have developed and applied a largely model independent fitting procedure which, at a given experimental  $(x_B, -t)$  kinematic point, takes the CFFs as free parameters and extracts them from DVCS observables using the well established QCD leading twist and leading order DVCS+BH theoretical amplitude. The expression of this amplitude can be found, for instance, in Ref. [18]. With this procedure, we have fitted in Ref. [16] the JLab Hall A proton DVCS beam-polarized and unpolarized cross sections. We could then extract the  $H_{Im}$  and  $H_{Re}$  CFFs at  $\langle x_B \rangle = 0.36$  and for several  $t$  values with average uncertainties of the order of 35% for  $H_{Im}$  and larger for  $H_{Re}$ . In Ref. [17], we have fitted several HERMES beam-charge, beam-spin and transversely polarized target spin asymmetries. We could then extract at  $\langle x_B \rangle = 0.09$  and for several  $t$  values, the same CFFs  $H_{Im}$  and  $H_{Re}$  with roughly similar uncertainties as for JLab.

The sources of uncertainty in our approach stem, on the one hand, from the experimental errors of the data that we fit, and on the other hand, from the fact that we take in

our fits practically all CFFs as free parameters, with relatively large and conservative bounds. There are therefore minimum conjectures and surmises in our work, which is certainly highly valuable. However, given that we generally fit limited sets of data and observables, our problem is in principle underconstrained. The consequence is that there are maximum correlations and interferences between our fitted parameters, hence the relatively important error bars in our results. In these extremely conservative conditions, it is nevertheless remarkable that we managed, in our previous works, to extract several CFFs, at different energies, with well-defined uncertainties, fitting the very limited available data. The reason for this convergence of a few CFFs, in spite of the underconstrained nature of the problem, is that some observables are in general dominated by some particular CFFs, like BSAs by  $H_{Im}$  and beam charge asymmetries and cross-sections by  $H_{Re}$ . Our uncertainties can only decrease in the future as, on the one hand, larger (and more precise) sets of data and observables sensitive to different CFFs become available and, on the other hand, theoretical constraints which allow to reduce, in the most model-independent way possible, the range of variation, or even the number, of the CFFs come forth (for instance, dispersion relations [19–22]).

We mention that related DVCS fitting studies have been published this past year [23, 24]. They resulted also in the extractions of the  $H_{Im}$  and  $H_{Re}$  CFFs with central values consistent with ours, although with smaller uncertainties. These fits are however model dependent. They either neglected all CFFs other than  $H_{Im}$  and  $H_{Re}$  or (and) assumed a functional shape for the CFFs, allowing to fit several  $(x_B, -t)$  points simultaneously. The uncertainty associated to the model dependence and hypothesis entering these approaches is then very difficult to estimate and to take into account properly. Nevertheless, each of these model-dependent and -independent approaches have their own merits and values. The fact that they all result in consistent and compatible central values for the fitted  $H_{Im}$  and  $H_{Re}$  CFFs gives mutual support and credit for each of them.

In this letter, we continue our model-independent fitting approach focusing this time on the CLAS BSAs and ITSAs, which we had not considered so far. As was already mentioned in our pioneer work on the subject [16], fitting only the CLAS BSAs, without any model-dependent hypothesis or input, was not constraining enough. In other words, fitting only BSAs, i.e. only one observable, with seven or eight unconstrained CFFs does not lead to well-defined solutions. However, inspired by our recent rather successful fit of a series of HERMES asymmetries [17], we now want to investigate if, with the addition of a new observable, namely the ITSAs, to be fitted simultaneously with the BSAs, progress can be made. Indeed, ITSAs have been measured by the CLAS collaboration as well and have actually received little attention from GPD phenomenologists so far. The BSAs being in general dominantly sensitive to

$H_{Im}$  and the ITSAs to  $\tilde{H}_{Im}$  [16, 25], our expectation is to extract some quantitative information on these two particular CFFs, which would be brand new information for  $\tilde{H}_{Im}$  in particular.

Let us describe these CLAS data. Regarding BSAs, the Hall B collaboration has measured their  $\phi$  distribution at 57  $(x_B, -t, Q^2)$  points ( $\phi$  is the standard angle between the leptonic and hadronic planes of the DVCS process). The values of the  $x_B$  variable extend from  $\approx 0.13$  up to  $\approx 0.46$ , those of the  $-t$  variable from  $\approx 0.13$  GeV<sup>2</sup> up to  $\approx 1.3$  GeV<sup>2</sup> and those of the  $Q^2$  variable from  $\approx 1.2$  GeV<sup>2</sup> up to  $\approx 3.3$  GeV<sup>2</sup>. The amplitude of these BSAs range from  $\approx 0$  up to  $\approx 0.3$  [10].

Regarding ITSAs, the data is much more scarce: in Ref. [12], only their  $\sin(\phi)$  moment is available at a few  $(x_B, -t, Q^2)$  points. The average kinematics of this whole set of data is  $\langle \xi \rangle = 0.16$  (i.e.  $\langle x_B \rangle \approx 0.275$ ),  $\langle -t \rangle = 0.31$  GeV<sup>2</sup> and  $\langle Q^2 \rangle = 1.82$  GeV<sup>2</sup>. Within this phase space, the ITSA  $\sin(\phi)$  moments (which we will designate as  $A_{UL}^{\sin\phi}$  following, for instance, Ref. [17]) have been extracted differentially, either for three  $x_B$  values ( $\approx 0.20, 0.29$  and  $0.40$ ) or for three  $-t$  values ( $\approx 0.15, 0.24$  and  $0.43$  GeV<sup>2</sup>). There are therefore six ITSAs available, which are actually not statistically independent since they are issued from the same set of data which has been binned either in  $x_B$  or in  $t$ . However, even if scarce, these data are extremely valuable as we will show in the following. Their amplitudes range from  $\approx 0.07$  to  $\approx 0.38$ , with uncertainties extending from 30% to more than 100%.

Following our notation of Ref. [17], the BSAs can also be denoted as  $A_{LU}$  and the ITSAs moments as  $A_{LU}^{\sin\phi}$ . We will use this notation on our figures.

In the first stage, we will see what information one can extract from the simultaneous fit of one ITSA and one BSA whose  $(x_B, -t, Q^2)$  values approximatively match. In the second stage, we will fit simultaneously one ITSA and the two or three BSAs which have the same  $(x_B, -t)$  values, irrespective of the  $Q^2$  value. Assuming the dominance of the QCD leading twist and leading order DVCS contribution, i.e. that CFFs do not depend on  $Q^2$ , the idea is to improve the statistical accuracy and increase the constraints on our fitting procedure.

Among the six available ITSAs, we first focus on the ITSA which has been measured at the kinematic point  $(x_B, -t, Q^2) = (0.29, 0.31, 1.82)$ . Unfortunately, the BSAs and the ITSAs are issued from two different Hall B experiments so that they have not been measured at exactly the same average kinematics. The matching of the kinematics between the different observables can thus be only approximate. Among the 57 BSAs, the two BSAs whose kinematics is the closest of the ITSA kinematics that we focus on, are at  $(0.25, 0.28, 1.69)$  and  $(0.25, 0.28, 1.95)$ . We therefore note at this stage the differences between the  $x_B$  values ( $0.25$  vs  $0.29$ ), the  $-t$  values ( $0.28$  vs  $0.31$ ) and  $Q^2$  values ( $1.69$  or  $1.95$  vs  $1.82$ ). There is a third BSA which

has the same  $x_B$  and  $t$  values as the two BSAs just mentioned but whose  $Q^2$  is equal to  $2.21$  GeV<sup>2</sup>. We will use this extra BSA in our  $Q^2$ -independent ‘‘second stage’’ fitting. We recapitulate these four kinematic points on which we presently focus in Table I.

	$\langle x_B \rangle$	$\langle -t \rangle$	$\langle Q^2 \rangle$
ITSA	0.29	0.31	1.82
BSA1	0.25	0.28	1.69
BSA2	0.25	0.28	1.95
BSA3	0.25	0.28	2.21

TABLE I: Summary of the four kinematical points which have approximately the same  $(x_B, -t)$  values. We will fit four ‘‘topologies’’: (ITSA+BSA1), (ITSA+BSA2), (ITSA+BSA3) and (ITSA+BSA1+BSA2+BSA3).

For the fitting procedure, as in Refs [16, 17], we minimize our theoretical calculations of the DVCS observables based on the well-known QCD leading twist and leading order DVCS+BH amplitude, by the standard  $\chi^2$  function, using MINUIT [26]. We recall that the parameters to be fitted are the CFFs of Eqs 1-8. As in Refs [16, 17], we have actually considered only seven CFFs, setting  $\tilde{E}_{Im}$  to zero. This is based on the theoretical guidance which approximates the  $\tilde{E}$  GPD by the pion exchange in the  $t$ -channel whose amplitude is real. With the hypothesis of the dominance of the leading twist amplitude of the DVCS process, this is the only model-dependent assumption that enters our fitting procedure. A last feature entering our fitting process is that we have to bound the domain of variation of the fitting parameters. Without bounds, our fits which are in general underconstrained, would probably not converge and/or would yield values for the fitted parameters with infinite uncertainties. Following what we have done and explained in details in Refs. [16, 17], we bound the allowed range of variation of the CFFs to  $\pm 5$  times some ‘‘reference’’ VGG CFFs. VGG [18, 27] is a well-known and widely used model which provides an acceptable first approximation of the CFFs, as shown in our previous studies [16, 17] and as will be confirmed furtherdown in the present work. We do not really consider this as a model-dependent input since this allowed deviation of a factor  $\pm 5$  with respect to the VGG model values is extremely conservative. We recall that GPDs have to satisfy a certain number of normalization constraints in general, these being all fulfilled by the VGG model. Finally, the problem at stake being non-linear and the parameters being correlated, we use MINOS for the uncertainty calculation on the resulting fitted parameters [26].

Before presenting our results, we also want to outline the point that our aim is to fit the ITSA and BSA(s) with the *same* CFFs, which therefore should correspond to unique  $(x_B, -t)$  values. As the data of Table I do not, unfortunately, have exactly the same kinematics, as mentioned previously, there is an ambiguity in defining the precise  $(x_B,$

$-t$ ) values of the fitted CFFs. We will consider that the CFFs that we will fit to the kinematic points of Table I correspond to the values of the BSA kinematics, i.e. (0.25, 0.28), as the BSA observable is in general the most significant statistically. There is clearly an approximation here, which we will make for the moment, lacking better solution, in order to make progress. This approximation is to some extent supported by the VGG model which predicts about 8% difference for  $H_{Im}$  between  $x_B=0.25$  and 0.29 (at  $-t=0.28$  GeV<sup>2</sup>) and less than 2% for  $H_{Im}$  for this same kinematic change. We stress that this kinematical matching problem is of a rather trivial nature and it is sufficient that future experiments, measuring different observables, simply agree to analyze data at the same central kinematics to avoid this extrapolation issue.

We now display in Fig. 2 the result of our fits. The left panel shows the  $\phi$  distribution of the three BSAs mentioned above and the right panel the  $\sin\phi$  moment of the ITSA. The dashed curves are the results of the fit of the ITSA (of the right panel) with each individual BSA. The thick solid curves are the result of the fit of this same ITSA with the three BSAs simultaneously (these three BSAs having the same  $(x_B, -t)$  values but different  $Q^2$  values, see Table I). On the right panel, the four empty circles show the corresponding results of the fit for the ITSA: the first three for the fit with the individual BSAs and the fourth one for the fit with the three BSAs simultaneously. For comparison, we also show in this figure the predicted results for the BSAs and the ITSA of the standard VGG model [18, 27]. It is seen that the VGG model overestimates the three BSAs by approximately 0.1 (i.e.  $\approx 30\%$ ) and underestimates the ITSA by roughly the same proportion.

We now show in Fig. 3 the fitted values, with their error bars, of the only two CFFs,  $H_{Im}$  and  $\tilde{H}_{Im}$ , out of seven, that came out of our fitting procedure with finite MINOS uncertainties. We recall that the MINOS uncertainties correspond to a deviation of 1 from the value which minimizes  $\chi^2$ . These uncertainties can be asymmetric if the  $\chi^2$  function is not symmetric around the minimum, which is the sign of a non-linear problem in general. The fact that only  $H_{Im}$  and  $\tilde{H}_{Im}$  converge in our fitting process reflects, as was mentioned earlier, the particular sensitivity of the BSA and ITSA observables, respectively, to these two CFFs. The other five CFFs did not converge in our fitting procedure to some well defined value or domain: either their central value reached the boundaries of the allowed domain of variation or MINOS could not reach the  $\chi^2+1$  value to fully determine the associated uncertainties. These features were well studied [16, 17] in our earlier works. They reflect the fact that the contribution to the  $\chi^2$  of those CFFs which did not converge is relatively weak and that the fit is barely sensitive to them. However, it is important to include them in our fit because they play a role, through correlations, in the determination of the error bars on the two “convergent” CFFs.

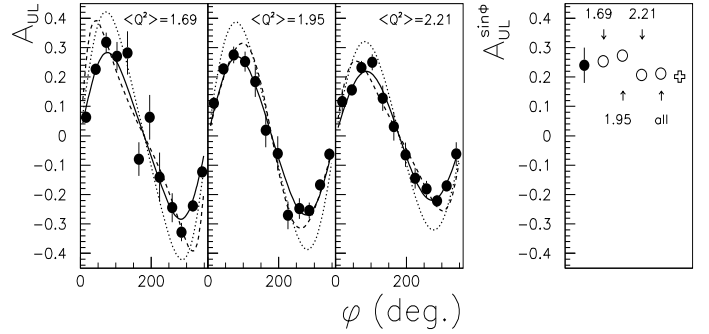


FIG. 2: Comparison of our fit results with the experimental data. The three left panels show the three experimental BSAs (i.e.  $A_{LU}$ ) as measured in Ref. [10] (solid circles). The right panel shows the experimental ITSA moment (i.e.  $A_{LU}^{\sin\phi}$ ) as measured in Ref. [12] (solid circle). The four panels correspond to the four  $(x_B, -t, Q^2)$  kinematic points presented in Table I (from left to right: BSA1, BSA2, BSA3 and ITSA). All four observables have approximately the same  $(x_B, -t)$  values, taken as (0.25, 0.28), but different  $Q^2$  values. On the BSA panels, the dashed solid curve is the result of our fit, fitting only the individual BSA of the relevant panel with the ITSA, i.e. from left to right, fit of (BSA1+ITSA), (BSA2+ITSA) and (BSA3+ITSA). The solid line is the result of our fit, fitting simultaneously the three BSAs and the ITSA, i.e. (BSA1+BSA2+BSA3+ITSA). This latter fit therefore assumes that CFFs do not depend on  $Q^2$ . The fit results of these four “topologies” for the ITSA are displayed in the right panel. On the BSA panels, the dotted curve is the prediction of the standard VGG model. Its prediction for the ITSA is displayed as the empty cross.

In Fig. 3, we display four sets of results for  $H_{Im}$  and  $\tilde{H}_{Im}$ , which correspond to the four “topologies” that we mentioned earlier: three sets correspond to the fits of the ITSA with each one of the BSAs at  $Q^2=1.69, 1.95$  and  $2.21$  GeV<sup>2</sup> and the fourth set (in the box in Fig. 3) corresponds to the simultaneous fit of the ITSA with the three BSAs. In this latter case, the underlying assumption is that CFFs do not depend on  $Q^2$ . As could be expected, the resulting uncertainties are smaller for the both CFFs in this latter configuration, as more statistics and constraints enter into play. We observe that all four configurations yield compatible results within error bars, which are between 25% and 50% in average. The simultaneous fit of the three BSAs and of the ITSA yields an approximate average of the fits using only one BSA and the ITSA. From the uncertainties on the CFFs that we obtain, it is clear that no QCD evolution or twist effect can be discerned. It then seems reasonable to fit simultaneously observables at the (approximately) same  $(x_B, -t)$  points and different  $Q^2$  values.

In Fig. 3, we have also displayed, for each of the four fit topologies, two results, aimed at illustrating the depen-

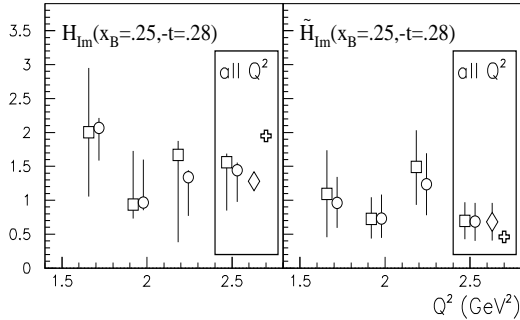


FIG. 3: Results of our fits to the data displayed in Fig. 3 for the  $H_{Im}$  and  $\tilde{H}_{Im}$  CFFs. The empty squares (circles) show our results when the boundary values of the domain over which the CFFs are allowed to vary is 5 (3) times the VGG reference values. Both results have been slightly shifted left (right) from the central  $Q^2$  value for sake of visibility. The four sets of results correspond, from left to right, to the fits (ITSA+BSA1), (ITSA+BSA2), (ITSA+BSA3) and (ITSA+BSA1+BSA2+BSA3) as indicated in Table I. In particular, the (ITSA+BSA1+BSA2+BSA3) fit, which corresponds to an average  $Q^2$  value of 1.95 GeV<sup>2</sup>, is displayed within a box. The empty diamond indicates the results of our fits, in the (ITSA+BSA1+BSA2+BSA3) “topology”, when only the  $H$  and  $\tilde{H}$  GPDs are taken as fitting parameters. The empty cross indicates the VGG prediction.

dence of our results on the boundaries of the domain of variation allowed for the CFFs. The empty squares show our results when the CFFs are limited to vary within  $\pm 5$  times the VGG reference values while the empty circles shows these results for boundaries equal to  $\pm 3$  times these same VGG reference values. Of course, the smaller the domain of variation, the smaller the uncertainties on the fitted CFFs. This shows the overall stability and robustness of our fitting process since the values of these boundaries do not affect strongly the central values of the fitted CFFs. We also checked that the fit results were not dependent on the precise starting values of the CFFs when we begin our fit: irrespective of the starting values, the minimization would essentially always converge to the same central values and uncertainties for  $H_{Im}$  and  $\tilde{H}_{Im}$ .

We further show in Fig. 3 the result of our fit if we take as fitting parameters only the  $H$  and  $\tilde{H}$  GPDs, i.e. four CFFs ( $H_{Re}$ ,  $\tilde{H}_{Re}$ ,  $H_{Im}$  and  $\tilde{H}_{Im}$ ), instead of seven. For this configuration, we have fitted the three BSAs and the ITSA simultaneously. The central values for  $H_{Im}$  and  $\tilde{H}_{Im}$  are in very good agreement with the ones previously determined when all CFFs were taken into account (with, though, a some slight decrease of the central value of  $H_{Im}$ ). The obvious difference is that, as could be expected, the associ-

ated uncertainties are smaller, particularly for  $H_{Im}$ . There is not too much effect for  $\tilde{H}_{Im}$ . This can probably be attributed to the fact that when only two GPDs enter the fit, the main source of uncertainty comes from the statistics of the observables to be fitted and no more from the correlations between the fitting parameters. Indeed,  $H_{Im}$  is mostly sensitive to the three BSAs (which are simultaneously fitted) with each having smaller errors than the ITSA, while  $\tilde{H}_{Im}$  is mostly sensitive to the ITSA which has a  $\approx 25\%$  error bar. We do not display the comparison of these “2 CFFs” fit with the data in Fig. 2 in order not to overload the figure, but the  $\chi^2$  is equally good to the fits with all CFFs. In the latter case, the normalized  $\chi^2$  is found to be equal to 1.27 while in the former case the normalized  $\chi^2$  is 1.16. These good results obtained when fitting with only  $H_{Im}$  and  $\tilde{H}_{Im}$  mean that it is indeed possible to correctly fit the data with only these two GPDs instead of four. This however does not mean that this is the true solution and that the other GPDs should consequently be ignored or neglected. The large error bars that we obtain when all GPDs precisely reflect this lack of knowledge on the other CFFs: our uncertainties incorporate all our ignorance about the other GPDs and all their full potential influence.

We finally display in Fig. 3 the predicted values of the corresponding VGG CFFs (empty crosses), which are  $Q^2$  independent. It is noted that the VGG  $H_{Im}$  tends to lie above the fitted  $H_{Im}$  while the VGG  $\tilde{H}_{Im}$  tends to lie below the fitted  $\tilde{H}_{Im}$ . This is a straightforward reflection of what was observed in Fig. 2 where the VGG BSAs curves were overestimating the data while the VGG ITSA point was underestimating the data. The overestimation of the VGG  $H_{Im}$ , with respect to the fitted central value, was also observed in our study of the HERMES data [17].

We have so far focused on the particular ITSA measured at  $x_B=0.29$  in order to establish and understand the basic features and results of our approach. We now turn to the ITSA measured at another  $x_B$  value, i.e.  $x_B=0.40$ , for which there are several BSAs which have neighboring ( $x_B$ ,  $-t$ ) values. These data points are indicated in Table II. This time, none of the  $Q^2$  values match each other and there is also a more significant difference between the  $x_B$  values. Supported by our previous study which showed that the simultaneous fits of several observables at different  $Q^2$ 's appeared to converge to some average of individual  $Q^2$  fits, we attempt to fit simultaneously the four data points (i.e. 3 BSAs and 1 ITSA) of Table II. We mention the VGG predictions: 13% change for  $H_{Im}$  between  $x_B=0.34$  and  $x_B=0.40$  (for  $-t=0.30$  GeV<sup>2</sup>) and 7% change for  $\tilde{H}_{Im}$  for the same kinematical variation. In front of the anticipated  $\approx 30\%$  error bars to be issued from our fits, it is not unreasonable to neglect, in a first approach, this small  $x_B$  variation.

Within this approximation, we are again able to extract values for the two CFFs  $H_{Im}$  and  $\tilde{H}_{Im}$  which we then consider to correspond to the BSAs' kinematics ( $x_B$ ,

	$\langle x_B \rangle$	$\langle -t \rangle$	$\langle Q^2 \rangle$
ITSA	0.40	0.31	1.82
BSA1	0.34	0.30	2.3
BSA2	0.34	0.28	2.63
BSA3	0.35	0.29	2.97

TABLE II: Selection of kinematic points measured by the CLAS collaboration which have approximately the same  $(x_B, -t)$  values, around  $x_B=0.35$ .

$-t)=(0.35, 0.29)$ , based on the statistical dominance of the BSAs. We show the resulting values of  $H_{Im}$  and  $\tilde{H}_{Im}$  in Table III, along with the values we obtained previously for these two CFFs at  $x_B=0.25$  when we fitted simultaneously all points of Table I (i.e. values of the data points in the ‘‘box’’ of Fig. 3). We observe, although error bars are not negligible, the general trend that, at fixed  $t$  ( $\approx 0.28$  GeV<sup>2</sup>),  $H_{Im}$  tends to increase, as  $x_B$  goes from 0.35 to 0.25, while  $\tilde{H}_{Im}$  remains rather constant.

$\langle x_B \rangle$	$H_{Im}$	$\tilde{H}_{Im}$
0.25	$1.56^{+0.12}_{-0.71}$	$0.69^{0.27}_{-0.27}$
0.35	$0.62^{+0.56}_{-0.18}$	$0.63^{+0.60}_{-0.32}$

TABLE III: Results of our fits for the  $H_{Im}$  and  $\tilde{H}_{Im}$  CFFs from the CLAS BSAs and ITSA, at fixed  $t \approx 0.28$  GeV<sup>2</sup>, for two different  $x_B$  values.

We recall that we were able in earlier work to also extract values for  $H_{Im}$  at different  $x_B$  values and at almost the  $t$  values considered here ( $\approx 0.28$  GeV<sup>2</sup>). For recall, in Ref. [16], we fitted the JLab Hall A data which have  $\langle x_B \rangle \approx 0.36$  and in Ref [17], we fitted the HERMES data which have  $\langle x_B \rangle \approx 0.09$ . While the JLab Hall A data were taken precisely at  $\langle -t \rangle = 0.28$  GeV<sup>2</sup>, the HERMES data were given for  $\langle -t \rangle = 0.20$  GeV<sup>2</sup> and  $\langle -t \rangle = 0.42$  GeV<sup>2</sup>. In a very simplistic way, we decide to interpolate between these two  $-t$  values by simply averaging our fitted  $H_{Im}$  CFFs at these two  $-t$  values. We also average quadratically the positive and negative error bars. We thus end up with some average HERMES  $H_{Im}$  CFF at  $\langle -t \rangle \approx 0.30$  GeV<sup>2</sup> and  $\langle x_B \rangle \approx 0.09$ . We can then obtain a  $x_B$  dependence of our fitted  $H_{Im}$ ’s using our JLab and HERMES analysis results. Fig. 4 shows this  $x_B$  dependence, compiling our results from the independent analysis of the JLab Hall A data, the HERMES data and the presently analyzed CLAS data.

It turns out that around  $x_B=0.35$ , both JLab Hall A and CLAS data are available. It is comforting to note the decent agreement, within error bars, of the two extracted values for  $H_{Im}$ . True, the error bars are not small and it might appear not so challenging to have an agreement with such uncertainties. Nevertheless, we would rather take this aspect as support for our realistic evaluation of the error bars on our fitted CFFs.

In order to illustrate this point, we also plot in Fig. 4

(open diamond around  $x_B=0.35$ ) our fit results of the CLAS BSAs and ITSA at  $x_B=0.35$  with only  $H$  and  $\tilde{H}$  as fitting parameters, i.e. four CFFs instead of seven. It is seen that the central value result which, as could be expected, has a quite smaller error bar, is slightly shifted with respect to the central value result when the seven CFFs are taken into account. However, both results remains well compatible within error bars. We did the same exercise with the JLab Hall A data at  $x_B=0.36$ . In Fig. 4, on the one hand, the open triangle shows the result of the fit to the JLab Hall A unpolarized and beam-polarized cross sections at  $\langle -t \rangle \approx 0.28$  GeV<sup>2</sup>, using only the  $H$  GPD, i.e. two CFFs. On the other hand, the open diamond around  $x_B=0.36$  the same fit using only  $H$  and  $\tilde{H}$ , i.e. four CFFs. Let us mention that these two fits give  $\chi^2$  values very close to one and describe very well the data points. Since these two fits use only a few CFFs, the error bars on the resulting  $H_{Im}$ ’s are quite (artificially ?) small compared to the error bar resulting from the fit with seven CFFs (open square). However, it is striking to see how the central value of  $H_{Im}$  can shift. With only  $H$  entering the JLab Hall A data fit,  $H_{Im}$  (open triangle near  $x_B=0.36$ ) is around two, at the top of the error bar of the seven CFFs fit result (open square near  $x_B=0.36$ ). This slight increase of  $H_{Im}$  is actually very consistent with the result of Ref. [23] which used the same assumption of  $H$  dominance. However, this result is now clearly inconsistent with the result for  $H_{Im}$  issued from our fit of the CLAS data (open square near  $x_B=0.35$ ).

Turning to the configuration where both  $H$  and  $\tilde{H}$  enter the fit of the same JLab Hall A data,  $H_{Im}$  has now dramatically dropped by a factor more than two (open diamond near  $x_B=0.36$ ). However, it has now actually become compatible with the result issued from the CLAS data, either open square or diamond near  $x_B=0.35$ . Indeed, note that both CLAS  $H_{Im}$  results, i.e. issued from the fit with only  $H$  on the one hand and with the seven CFFs on the other hand, are compatible within error bar. This is a clear-cut illustration of the meaning of the large error bars which result from our fits when we use seven CFFs: they cautiously and realistically reflect the underconstrained nature of our problem, i.e. fitting only a couple of observables with many parameters (i.e. the CFFs), and all the variation and potential weight of these parameters.

To summarize this discussion, in the framework of our analysis (i.e. leading twist and leading order QCD and the few kinematic approximations mentioned earlier), it doesn’t seem to us possible to find a consistent value of  $H_{Im}$  to fit both the JLab Hall A and CLAS data if only  $H$  enters the fit. The minimum scenario seems that  $\tilde{H}$  be included, the ultimate one being of course that all CFFs be included. It is interesting to mention that Ref. [24] reached some similar conclusion in a model-dependent approach, confirming the hint that GPDs other than  $H$  (and possibly  $\tilde{H}$ ) do play a significant role at the JLab kinematics. Let us stress again that at this kinematic point,  $\langle x_B \rangle \approx 0.35$ ,

our values of  $H_{Im}$  were determined by the fitting of independent DVCS experiments, i.e. JLab Hall A and CLAS, and rather different observables: polarized and unpolarized cross sections for the JLab Hall A analysis and BSA and ITSA for the present CLAS analysis. Although beam polarized observables are common to the two experiments, it is encouraging to observe that different paths can lead to consistent results, as it should be.

Now, more generally, taking into account the HERMES data, we observe in Fig. 4 that the general tendency is that, at fixed  $t$ ,  $H_{Im}$  increases with decreasing  $x_B$ . This is reminiscent of the  $x_B$  dependence of standard parton distributions. The VGG prediction is also shown in Fig. 4 and, although it overestimates most of the fitted central values, it displays the same behavior.

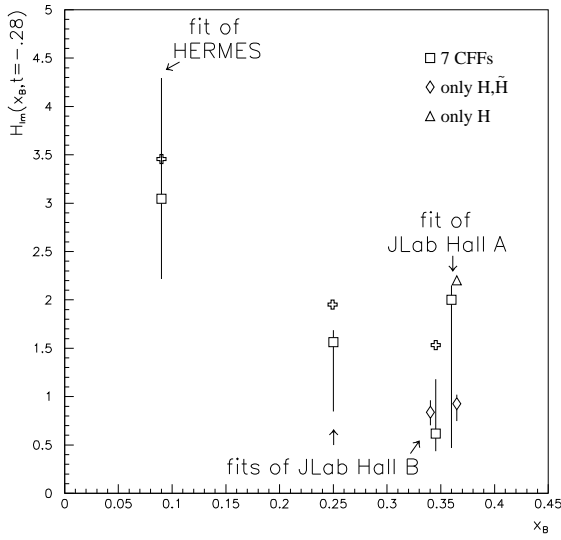


FIG. 4:  $x_B$  dependence at fixed  $-t=0.28$  GeV<sup>2</sup> of the fitted  $H_{Im}$  (empty squares) according to our analyzes of the JLab Hall A data [16] ( $\langle x_B \rangle \approx 0.36$ ), of the HERMES data [17] ( $\langle x_B \rangle \approx 0.09$ ) and of the present analysis ( $\langle x_B \rangle \approx 0.25$  and  $\langle x_B \rangle \approx 0.35$ ), using the seven CFFs. The open diamond, slightly shifted left (for visibility) of the open square point at  $x_B \approx 0.35$  is the result of the CLAS BSAs and ITSA at  $x_B \approx 0.35$  using only the  $H$  and  $\tilde{H}$  GPDs. The open triangle, slightly shifted right (for visibility) of the open square point at  $x_B \approx 0.36$  is the result of the JLab Hall A unpolarized and beam-polarized cross sections at  $x_B=0.36$  using only the  $H$  GPD. The open diamond, slightly shifted right (for visibility) of the open square point at  $x_B \approx 0.36$  is the result of the JLab Hall A unpolarized and beam-polarized cross sections at  $x_B=0.36$  using only the  $H$  GPD and  $\tilde{H}$  GPDs. The empty cross indicates the VGG prediction.

We now finally turn our attention to the  $t$  dependence of the ITSAs. The CLAS collaboration has extracted the ITSAs at fixed  $x_B$  ( $\approx 0.25$ ) for three different  $\langle -t \rangle$  values: 0.15, 0.24 and 0.43 GeV<sup>2</sup>. For each of these  $-t$  points, we can identify three BSAs which have approximately the

same  $x_B$  and  $-t$  values with, however, different  $Q^2$  values. We list those points in table IV. Comforted by our reasonable results presented in Fig. 3, we adopt the same approach and fit, with the seven CFFs as fitting parameters, simultaneously the three BSAs and the ITSA at each of the three  $(x_B, -t)$  points of Table IV, which all have a common  $x_B$  value (i.e.  $\approx 0.25$ ). Again, only the  $H_{Im}$  and  $\tilde{H}_{Im}$  CFFs systematically come out from our fits with finite error bars. Fig. 5 shows our results and reveals the  $t$ -dependence (at  $x_B \approx 0.25$ ) of the  $H_{Im}$  and  $\tilde{H}_{Im}$  CFFs. We again display for each  $t$  value two results corresponding, like in Fig. 3, to different boundary values for the domain of variation allowed for the CFFs, i.e.  $\pm 5$  (empty squares) and  $\pm 3$  (empty circles) times the VGG reference values. We also show in this figure the VGG predictions (empty crosses).

	$\langle x_B \rangle$	$\langle -t \rangle$	$\langle Q^2 \rangle$
ITSA	0.27	0.15	1.82
BSA1	0.24	0.15	1.65
BSA2	0.24	0.14	1.89
BSA3	0.25	0.14	2.16
ITSA	0.27	0.24	1.82
BSA1	0.25	0.28	1.69
BSA2	0.25	0.28	1.95
BSA3	0.25	0.28	2.21
ITSA	0.27	0.43	1.82
BSA1	0.25	0.49	1.70
BSA2	0.25	0.49	1.95
BSA3	0.25	0.49	2.20

TABLE IV: Selection, for our  $t$ -dependence study, of the three  $(x_B, -t)$  kinematic points measured by the CLAS collaboration which have 1 ITSA and 3 BSAs at approximately the same  $x_B$  values ( $\approx 0.25$ ).

In Fig. 5, regarding  $H_{Im}$ , we note a smooth and typical fall-off with  $-t$  which was also observed in our previous JLab Hall A and HERMES studies [16, 17]. The figure also confirms that the standard VGG parametrisation, in general, overestimates our fitted values. This is particularly the case at low  $t$  (this was also observed at HERMES energies [17]). Regarding  $\tilde{H}_{Im}$ , although the uncertainties are large, the  $t$ -slope appears to be much less pronounced and it even seems that there is a drop towards 0 as  $t$  goes to 0 (although a constant and flat  $t$ -dependence can also be in order within error bars). We find again that VGG underestimates this CFF, in particular as  $|t|$  grows. Overall, the VGG  $t$ -slope is markedly different from the one of the fitted  $\tilde{H}_{Im}$ .

Finally, the diamonds in Fig. 5 show the results of our fit when only the  $H$  and  $\tilde{H}$  GPDs are taken as fitting parameters, i.e. setting to 0 all other GPDs. We observe the same features as previously (see Fig. 3). The central values are in very good agreement with the ones determined

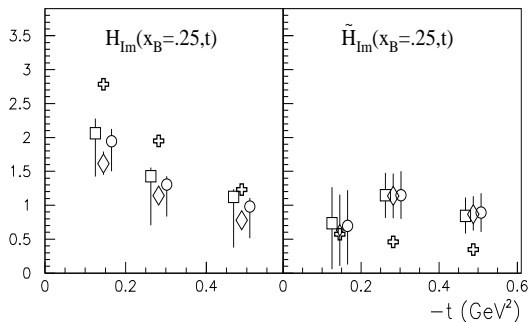


FIG. 5:  $t$ -dependence of our fitted  $H_{Im}$  and  $\tilde{H}_{Im}$  CFFs at the kinematic points of Table IV. The empty squares (circles) show our results when the boundary values of the domain over which the CFFs are allowed to vary is 5 (3) times the VGG reference values. The empty diamonds indicate the results of our fits when only the  $H$  and  $\tilde{H}$  GPDs are taken as fitting parameters. The empty crosses indicate the VGG prediction. At the lowest  $t$  value of  $\tilde{H}_{Im}$ , the empty cross and diamond happen to be superimposed.

from the fits in which all CFFs were included (though with a systematic decrease by  $\approx$  of 15% of the central value of  $H_{Im}$ ). The main effect is to reduce the uncertainties on the fitted CFFs: very strongly for  $H_{Im}$  and only slightly for  $\tilde{H}_{Im}$ .

To summarize this work, we have analyzed the beam spin asymmetry and the longitudinally polarized target spin asymmetry of the Deep Virtual Compton Scattering process recently measured by the CLAS collaboration. We have used a fitter code, largely model-independent, based on the QCD leading-twist and leading order DVCS+BH amplitude, which takes as fitting parameters GPD CFFs. Even though we fit only two asymmetry observables with seven CFFs, two CFFs,  $H_{Im}$  and  $\tilde{H}_{Im}$ , come out systematically from our fits with stable and well defined central values and uncertainties (of the order of 30% in average). The reason is that the two observables we fit are well known to be dominantly sensitive to these two CFFs. It is worth noting that with only BSAs to fit, there is no convergence of our fits, while with the addition of a single observable, i.e. the ITSA, solutions become relatively well defined.

In this work, a few approximations have been made, mostly due to the present lack of sufficiently precise and numerous data. We recall that only six ITSAs were available to us: for three  $-t$  values at fixed  $x_B$  and  $Q^2$  and for three  $x_B$  values at fixed  $-t$  and  $Q^2$  values. The approximations that we did were to simultaneously fit BSAs and ITSAs taken at slightly different  $x_B$  and  $-t$  values and also at different  $Q^2$  values. This latter approximation is, in any case, along the line of the main starting assumption of this

work: the dominance of the QCD leading twist and leading order of the DVCS amplitude. In those conditions, we have been able to determine the  $x_B$ - and  $t$ -dependences of the  $H_{Im}$  and  $\tilde{H}_{Im}$  CFFs (respectively at fixed  $t$  and fixed  $x_B$ ). In particular, we put in evidence a much flatter  $t$ -dependence for  $\tilde{H}_{Im}$  than for  $H_{Im}$ . We also illustrated, by comparing our fits at roughly the same kinematics of the independent JLab Hall A and CLAS data, the importance and, even the necessity, of taking into account several GPDs in order to obtain compatible results.

While there have lately been a couple of other works aiming at fitting DVCS data and extracting  $H_{Im}$ , this is the first one allowing access to  $\tilde{H}_{Im}$  and, in a largely model-independent way, determine some first numerical value for it. The “price” to pay for our model-independency is that we obtain relatively large uncertainties. Several DVCS experiments aiming at measuring more precisely the observables analyzed in this work and also aimed at measuring new observables, such as transversely polarized target spin asymmetries and cross sections are under way in the near future. We expect our fitting techniques to be more and more fruitful and efficient as these new precise and numerous data become available, along with theoretical GPD modelling progress which can reduce the domain of variation of the fitted CFFs or their number.

- 
- [1] D. Müller, D. Robaschik, B. Geyer, F.-M. Dittes, and J. Horejsi, *Fortschr. Phys.* **42**, 101 (1994).
  - [2] X. Ji, *Phys. Rev. Lett.* **78**, 610 (1997); *Phys. Rev. D* **55**, 7114 (1997).
  - [3] A.V. Radyushkin, *Phys. Lett. B* **380** (1996) 417; *Phys. Rev. D* **56**, 5524 (1997).
  - [4] J.C. Collins, L. Frankfurt and M. Strikman, *Phys. Rev. D* **56**, 2982 (1997).
  - [5] K. Goeke, M. V. Polyakov and M. Vanderhaeghen, *Prog. Part. Nucl. Phys.* **47**, 401 (2001).
  - [6] M. Diehl, *Phys. Rept.* **388**, 41 (2003).
  - [7] A.V. Belitsky, A.V. Radyushkin, *Phys. Rept.* **418**, 1 (2005).
  - [8] S. Boffi and B. Pasquini, *Riv. Nuovo Cim.* **30**, 387 (2007).
  - [9] C. Muñoz Camacho et al., *Phys. Rev. Lett.* **97**, 262002 (2006).
  - [10] F.-X. Girod et al., *Phys. Rev. Lett.* **100**, 162002 (2008).
  - [11] S. Stepanyan et al., *Phys. Rev. Lett.* **87**, 182002 (2001).
  - [12] S. Chen et al., *Phys. Rev. Lett.* **97**, 072002 (2006).
  - [13] A. Airapetian et al., *Phys. Rev. Lett.* **87**, 182001 (2001).
  - [14] A. Airapetian et al., *JHEP* **0806**, 066 (2008).
  - [15] A. Airapetian et al., *JHEP* **0911**, 083 (2009).
  - [16] M. Guidal, *Eur. Phys. J. A* **37**, 319 (2008), *Erratum-ibid.*A40:119,2009.
  - [17] M. Guidal and H. Moutarde, *Eur. Phys. J. A* **42**, 71 (2009).
  - [18] M. Vanderhaeghen, P.A.M. Guichon, M. Guidal, *Phys. Rev. D* **60**, 094017 (1999).
  - [19] O. V. Teryaev, proceedings of 11th International Conference on Elastic and Diffractive Scattering: Towards High Energy Frontiers, Blois, France, 15-20 May 2005, arXiv:0510.031

- [hep-ph].
- [20] K. Kumericki, D. Muller and K. Passek-Kumericki, Nucl. Phys. B **794**, 244 (2008).
- [21] M. Diehl and D. Y. Ivanov, Eur. Phys. J. C **52**, 919 (2007).
- [22] I. V. Anikin and O. V. Teryaev, proceedings of the International Conference on Hadron Structure (HS07), Modra-Harmonia, Slovakia, 3-7 September 2007, arXiv:0710.4211 [hep-ph].
- [23] H. Moutarde, Phys. Rev. D **79**, 094021 (2009).
- [24] K. Kumericki and D. Müller, arXiv:0904.0458 [hep-ph].
- [25] A. Belitsky, D. Muller and A. Kirchner, Nucl. Phys. B **629**, 323 (2002).
- [26] F. James, MINUIT, D507, CERN (1978).
- [27] M. Guidal, M. V. Polyakov, A. V. Radyushkin and M. Vanderhaeghen, Phys. Rev. D **72**, 054013 (2005).